

Bi-CamoDiffusion: A Boundary-informed Diffusion Approach for Camouflaged Object Detection

Patricia L. Suarez¹ Leo Thomas Ramos^{2,3} Angel D. Sappa^{1,2,3}

¹ESPOL Polytechnic University ²Computer Vision Center ³Universitat Autònoma de Barcelona

plsuarez@espol.edu.ec; ltramos@cvc.uab.cat; sappa@ieee.org

Abstract

Bi-CamoDiffusion is introduced, an evolution of the CamoDiffusion framework for camouflaged object detection. It integrates edge priors into early-stage embeddings via a parameter-free injection process, which enhances boundary sharpness and prevents structural ambiguity. This is governed by a unified optimization objective that balances spatial accuracy, structural constraints, and uncertainty supervision, allowing the model to capture of both the object’s global context and its intricate boundary transitions. Evaluations across the CAMO, COD10K, and NC4K benchmarks show that Bi-CamoDiffusion surpasses the baseline, delivering sharper delineation of thin structures and protrusions while also minimizing false positives. Also, our model consistently outperforms existing state-of-the-art methods across all evaluated metrics, including S_m , F_β^w , E_m , and MAE, demonstrating a more precise object-background separation and sharper boundary recovery.

1. Introduction

Camouflaged Object Detection (COD) involves the pixel-level localization of objects whose appearance exhibits extremely low foreground-background separability [8, 11]. The objective is to generate accurate segmentation masks under these conditions [25], enabling reliable object delineation even when visual evidence is weak. Unlike conventional segmentation settings that rely on dominant visual cues [23], COD addresses scenarios in which object presence must be inferred from subtle structural and contextual signals [25, 35].

COD is challenging due to multiple factors, including intrinsic target-background similarity [8], large variations in object scale [1], and frequent occlusions disrupting spatial continuity [7]. Beyond these, a key challenge lies in the reliable delineation of object boundaries [7, 37]. When visual transitions are weak or fragmented, determining where the object ends becomes uncertain, often leading to unsta-

ble masks and imprecise spatial support [27]. Consequently, boundary ambiguity emerges as a central obstacle in accurate COD.

Diverse strategies have been proposed for COD, including Convolutional Neural Networks (CNN), attention-driven models [13, 40], and more recently, generative frameworks [13]. Among these, diffusion models have gained particular relevance by formulating the prediction as an iterative denoising process [10, 24, 26]. However, diffusion models present certain limitations, as they do not explicitly enforce structural constraints [17] during mask formation. Consequently, predictions may produce plausible regions but fail to preserve rigid geometric structures [32], a deficiency that becomes critical when precise boundary delineation is required.

Based on the above, and building upon CamoDiffusion [2], a structurally informed extension designed to improve boundary delineation is introduced. The proposed approach incorporates structural cues directly into the early feature space, enabling the denoising process to better preserve spatial support as the mask progressively emerges. This reinforces contour fidelity in visually ambiguous regions. The approach preserves the generative process without altering the underlying backbone, maintaining architectural compatibility.

To further support boundary delineation, a multi-scale boundary-informed objective is proposed. The loss extends the base diffusion segmentation supervision with three complementary four applied across output scales: a focal structure component that emphasizes hard pixels while preserving region level structure, a boundary term that enforces contour agreement between predictions and ground-truths, and an uncertainty aware regularization term that penalizes ambiguous responses to stabilize optimization. Also, an RGB boundary consistency constraint aligns predicted contours with structural cues derived from the input image, reducing boundary bleeding.

Experiments on the CAMO, COD10K, and NC4K datasets demonstrate that the proposed approach achieves consistent improvements in detection quality, producing

sharper contours and more reliable predictions in challenging camouflaged scenes. The main contributions of this work are summarized as follows:

- A structurally informed extension of CamoDiffusion to improve boundary delineation during diffusion-based mask prediction.
- A multi-scale boundary-informed training objective that promotes contour aligned predictions and stabilizes structural consistency.
- Evaluation across multiple COD benchmarks demonstrating improved boundary fidelity and detection reliability.

2. Related work

Early COD methods primarily relied on CNN architectures to enhance structural perception through progressive refinement and feature aggregation. Multi-stage pipelines [28], graph-based reasoning [37], and rank-oriented supervision [15] have been explored to improve localization under weak foreground-background separability. Subsequent efforts placed greater emphasis on boundary sensitivity, incorporating contour-focused supervision [16], feature decomposition [8], and frequency-aware representations [3] to better capture subtle signal variations often concealed by camouflage. Despite these advances, most CNN-based designs remain largely dependent on deterministic feature learning, where structural cues are recovered indirectly through refinement rather than explicitly enforced during prediction.

Transformer-based models introduced stronger global reasoning capabilities, enabling the modelling of long-range dependencies. Uncertainty-guided attention has been explored to improve robustness in visually ambiguous regions [34], while collaborative pyramid modelling supports multi-scale token interaction [21]. Masked separable attention further enhances region isolation by limiting cross-token interference [36]. Recent work integrates frequency-spatial representations through entanglement transformer blocks [30] and incorporates external knowledge via text-guided interaction and adaptive data selection [33] to enhance discrimination. Despite improved semantic coherence, boundary ambiguity remains a persistent challenge, suggesting that global context alone does not fully resolve the structural uncertainty inherent to camouflaged scenes.

Generative formulations have recently reframed COD as a probabilistic generation task, allowing predictions to emerge through iterative refinement rather than deterministic decoding. Diffusion-based models exemplify this shift by progressively denoising mask representations [2]. Data-centric strategies further enhance robustness by synthesizing harder camouflaged training samples to expand supervision under challenging visual conditions [9]. In parallel, low-supervision paradigms explore noise-tolerant learning through noisy pseudo labels [38] and retrieval-based self-augmentation to stabilize training without ground-truth

masks [4]. Nevertheless, structural constraints are rarely integrated explicitly into the generative process, leaving boundary formation dependent on emergent behaviour.

Across these research lines, a consistent trend emerges toward improving mask coherence through stronger contextual modelling, structural priors, and generative refinement. However, structural constraints often remain implicitly encoded within the learning process rather than explicitly integrated into mask formation itself. As a result, boundary delineation continues to depend on emergent behaviour instead of direct structural guidance, leaving room for approaches that more tightly couple contour evidence with the generative dynamics of prediction.

3. Proposed approach

3.1. Overview

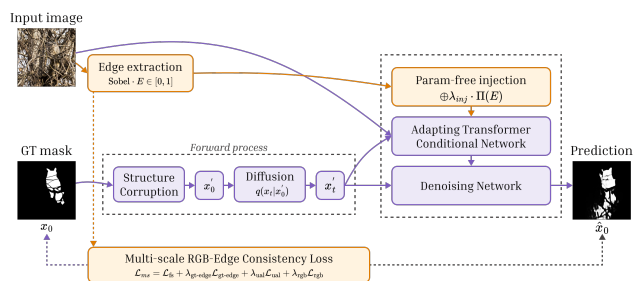


Figure 1. High-level overview of the proposed Bi-CamoDiffusion. Components highlighted in orange represent the contributions introduced in this work, while purple denotes the original CamoDiffusion components.

We build on CamoDiffusion [2], which formulates COD as conditional denoising diffusion for segmentation. Let I denote an RGB image and y the ground-truth binary mask. During training, a forward noising (corruption) process gradually perturbs the clean target y into a noisy variable $x_t \sim q(x_t | y, t)$ at diffusion step t . The diffusion model f_θ then learns to invert this process by predicting the clean mask variable x_0 from the noisy input x_t , conditioned on the image I and the timestep t , so that $\hat{x}_0 = f_\theta(x_t, I, t)$.

The proposed model extends CamoDiffusion with a boundary-informed design that introduces no additional learnable parameters and remains compatible with pre-trained weights. The key idea is to exploit an RGB edge prior E (computed once per image and provided during both training and inference) to encourage sharper contours without altering the backbone design. As illustrated in Fig. 1, E is incorporated through two complementary components:

- **Boundary feature injection**, a parameter-free additive modulation applied to the earliest feature embedding stage, which biases low-level representations toward boundary cues.

- **Boundary alignment loss**, an auxiliary supervision term that penalizes mismatch between the predicted mask gradients and the RGB edge prior.

These components sharpen contours and reduce boundary bleeding. Bellow, each component is described in detail.

3.2. Edge prior construction and feature injection

Grayscale conversion Given an RGB image $I \in \mathbb{R}^{3 \times H \times W}$ with channels $I_R, I_G, I_B \in \mathbb{R}^{H \times W}$, first a single-channel luminance map via the standard ITU-R BT.601 weighted conversion is obtained, as in Eq. (1):

$$G = \mathcal{G}(I) = 0.299 I_R + 0.587 I_G + 0.114 I_B, \quad G \in \mathbb{R}^{H \times W}. \quad (1)$$

This projection suppresses chromatic variation and retains only luminance structure, which is the dominant perceptual cue for spatial discontinuities. Crucially, camouflage patterns exploit colour and texture mimicry, but intensity transitions at object boundaries remain detectable even in hard-camouflage scenes. Operating on G rather than directly on I thus reduces sensitivity to misleading chromatic gradients in the background.

Sobel edge magnitude The edge prior E is obtained by applying the Sobel operator to G . The two directional gradient responses are computed via fixed 3×3 convolution kernels shown in Eq. (2):

$$\mathbf{K}_x = \begin{pmatrix} -1 & 0 & 1 \\ -2 & 0 & 2 \\ -1 & 0 & 1 \end{pmatrix}, \quad \mathbf{K}_y = \begin{pmatrix} -1 & -2 & -1 \\ 0 & 0 & 0 \\ 1 & 2 & 1 \end{pmatrix}, \quad (2)$$

yielding horizontal and vertical gradient maps $\partial_x G = \mathbf{K}_x * G$ and $\partial_y G = \mathbf{K}_y * G$, where $*$ denotes spatial convolution with unit-stride and same-padding. The edge magnitude is then defined as in Eq. (3):

$$E = \mathcal{S}(G) = \sqrt{(\partial_x G)^2 + (\partial_y G)^2 + \varepsilon}, \quad E \in [0, 1], \quad (3)$$

where $\varepsilon > 0$ is a small constant for numerical stability. The result is clipped to $[0, 1]$ to produce a normalised boundary map. The complete extraction pipeline is therefore established as shown in Eq. (4):

$$E = \mathcal{S}(\mathcal{G}(I)), \quad (4)$$

which is parameter-free and differentiable everywhere except at exact zero-gradient locations.

The backbone follows a hierarchical patch-embedding design in which the first stage \mathcal{C}_1 operates at the highest spatial resolution and captures fine-grained structural detail. Subsequent stages progressively downsample features

and shift representation toward higher-level semantics, irreversibly discarding precise spatial support in the process.

Injecting edge information at the earliest stage therefore ensures that boundary cues influence all subsequent feature transformations, rather than being introduced as a correction after spatial detail has already been discarded. Furthermore, operating at the earliest stage keeps the injection localised to a single, well-defined intervention point, making the design transparent and easy to ablate.

Parameter-free feature modulation Let $F_1 = \mathcal{C}_1(I) \in \mathbb{R}^{B \times C \times H' \times W'}$ denote the feature map produced by the first convolutional stage, where C is the embedding dimension and $H' = \lfloor H/s \rfloor$, $W' = \lfloor W/s \rfloor$ are the spatially downsampled dimensions with stride s . A modulated feature map \tilde{F}_1 is defined as in Eq. (5):

$$\tilde{F}_1 = F_1 + \lambda_{\text{inj}} \cdot \Pi(E), \quad (5)$$

where $\lambda_{\text{inj}} \in \mathbb{R}_{>0}$ is a fixed scalar hyperparameter and $\Pi : \mathbb{R}^{1 \times H \times W} \rightarrow \mathbb{R}^{C \times H' \times W'}$ is a deterministic, parameter-free operator defined as in Eq. (6):

$$\Pi(E) = \mathbf{1}_C \otimes \phi(E), \quad (6)$$

with $\phi(E) \in \mathbb{R}^{1 \times H' \times W'}$ denoting nearest-neighbour spatial rescaling of E to the target resolution, and \otimes denoting channel-wise broadcasting (i.e., replication across the C dimension). No learnable projection is introduced, so the modulation carries no trainable parameters.

The additive form in Eq. (5) is deliberate as an additive bias of this form can be interpreted as shifting the effective input to each downstream transformer block toward regions of high boundary activity, without distorting the feature distribution learned during pretraining. In contrast, approaches such as channel-wise gating or feature concatenation would either require new parameters or alter the input dimensionality seen by subsequent layers, both of which break compatibility with pretrained backbone weights.

Boundary-sharpening pre-filter The Sobel response E measures gradient magnitude over a 3×3 neighbourhood, which can yield spatially thick activations around boundaries. To obtain a sharper and more precisely localised boundary signal prior to injection, a fixed discrete Laplacian operator \mathbf{K}_L to E before channel expansion can be applied. The Laplacian kernel used is shown in Eq. (7):

$$\mathbf{K}_L = \begin{pmatrix} 0 & 1 & 0 \\ 1 & -4 & 1 \\ 0 & 1 & 0 \end{pmatrix}, \quad (7)$$

and the sharpened signal is shown in Eq. (8):

$$\phi(E) = \left| \mathbf{K}_L * \tilde{E} \right|, \quad (8)$$

where \tilde{E} is E rescaled to $H' \times W'$ and $|\cdot|$ denotes element-wise absolute value, which retains responses of both polarities. As a second-order derivative operator, the Laplacian responds maximally at zero-crossings of intensity transitions, precisely where object boundaries are located, and produces thin, well-localised activations compared to the first-order Sobel response. Since \mathbf{K}_L is a fixed constant kernel, this step introduces no additional parameters and does not affect backbone compatibility. The full modulated representation \tilde{F}_1 is then forwarded unchanged to the remaining stages of the backbone.

3.3. Multi-scale RGB-Edge Consistency Loss

While the parameter-free feature modulation introduced in this work biases the network representation toward boundary cues, this alone does not guarantee that the predicted mask contours align with the edge structure of the input. To close this gap, a Multi-scale RGB-Edge Consistency Loss is proposed, which is a composite training objective that combines region-level segmentation accuracy with explicit boundary constraints derived directly from the input image. The loss is organised around four complementary terms, each targeting a distinct aspect of boundary quality in diffusion-based COD, and is evaluated jointly across multiple spatial scales. Each component is described below.

Focal-structure loss The base segmentation term must handle two concurrent challenges: hard pixels near camouflage boundaries where the model is most uncertain, and the structural bias toward under-segmenting thin or elongated regions. Both are addressed with a compound loss that fuses a boundary-weighted focal cross-entropy with a weighted Intersection over Union (IoU) term.

Let $\hat{y} = \sigma(z) \in [0, 1]^{H \times W}$ denote the predicted probability map obtained by applying the sigmoid σ to the logit output z , and let $y \in \{0, 1\}^{H \times W}$ be the ground-truth mask. A spatially adaptive weight map that emphasises pixels in the vicinity of object boundaries is defined, as in Eq. (9):

$$w(y) = 1 + \alpha |\bar{y} - y|, \quad \bar{y} = \text{AvgPool}_k(y), \quad (9)$$

where AvgPool_k denotes average pooling with kernel size $k = 31$ and same-padding, and $\alpha = 5$. The difference $|\bar{y} - y|$ is large precisely at boundary pixels and small in homogeneous interior or background regions, so $w(y)$ concentrates supervision where it is most needed.

The boundary-weighted focal cross-entropy is then defined in Eq. (10):

$$\mathcal{L}_{\text{fbce}}(z, y) = \frac{\sum_i w_i \cdot (1 - p_t^i)^\gamma \cdot \text{BCE}(z_i, y_i)}{\sum_i w_i + \varepsilon}, \quad (10)$$

where $p_t^i = \hat{y}_i \cdot y_i + (1 - \hat{y}_i)(1 - y_i)$ is the probability assigned to the correct class at pixel i , $\gamma = 2$ is the focus-

ing exponent, and $\text{BCE}(\cdot, \cdot)$ denotes binary cross-entropy. The factor $(1 - p_t^i)^\gamma$ down-weights well-classified pixels and forces the model to focus on the hard boundary pixels already emphasised by w .

The complementary weighted IoU term penalises region-level under-segmentation, as shown in Eq. (11):

$$\mathcal{L}_{\text{wIoU}}(z, y) = 1 - \frac{\sum_i w_i \hat{y}_i y_i + 1}{\sum_i w_i (\hat{y}_i + y_i) - \sum_i w_i \hat{y}_i y_i + 1}, \quad (11)$$

where the $+1$ Laplace smoothing prevents division by zero on empty predictions. The full focal-structure loss given by Eq. (12):

$$\mathcal{L}_{\text{fs}} = \mathcal{L}_{\text{fbce}} + \mathcal{L}_{\text{wIoU}}. \quad (12)$$

Ground-truth edge loss Even with the focal weighting above, the loss operates on per-pixel classification values and does not directly penalise errors in the spatial gradient of the prediction. A mask that is correct on average but blurred at boundaries will incur low \mathcal{L}_{fs} yet fail precisely at contours. This is addressed by directly supervising the gradient field of the prediction. Let $\mathcal{S}(\cdot)$ denote the Sobel magnitude operator defined in Eq. (3). The ground-truth edge term is defined in Eq. (13):

$$\mathcal{L}_{\text{gt-edge}}(z, y) = \|\mathcal{S}(\hat{y}) - \mathcal{S}(y)\|_1, \quad (13)$$

which penalises the ℓ_1 distance between the Sobel response of the predicted probability map and the Sobel response of the binary ground-truth mask. This formulation is differentiable with respect to z via $\hat{y} = \sigma(z)$ and the Sobel convolutions, allowing gradients to flow directly into the network from edge misalignment errors.

Uncertainty-aware loss Diffusion-based models introduce intermediate denoising states x_t that are inherently noisy, producing predictions with spatially uneven confidence. Pixels where the model is uncertain, i.e., where $\hat{y}_i \approx 0.5$, should be penalised more aggressively to encourage the model to resolve ambiguity rather than maintain soft, indeterminate predictions. Therefore, the uncertainty map is given by Eq. (14):

$$u_i = 1 - |2\hat{y}_i - 1|^2 \in [0, 1], \quad (14)$$

which attains its maximum value of 1 when $\hat{y}_i = 0.5$ (maximally uncertain) and is zero for fully confident predictions ($\hat{y}_i \in \{0, 1\}$). The uncertainty-aware loss then uses this map as a spatially-varying penalty weight given by Eq. (15):

$$\mathcal{L}_{\text{ual}}(z, y) = \frac{1}{HW} \sum_i u_i, \quad (15)$$

encouraging the network to reduce spatial uncertainty globally and converge to more decisive, sharply-bounded predictions. This term is particularly important during early diffusion timesteps, when x_t is highly corrupted and the model must learn to produce meaningful predictions despite noisy intermediate states.

RGB-Edge Consistency Loss The three terms above rely exclusively on ground-truth mask annotations for boundary supervision. However, the mask annotation itself may be imprecise near ambiguous boundaries, and it carries no information about the image evidence supporting each predicted contour. For this, an additional supervision signal derived directly from the input image (the RGB edge prior E defined in Eq. (4)) is introduced. Rather than enforcing that the prediction matches E pixel-wise, which would conflate all image gradients with object boundaries, the gradient field of the prediction is aligned with E using Eq. (16):

$$\mathcal{L}_{\text{rgb}}(z, E) = \|\mathcal{S}(\hat{y}) - \tilde{E}\|_1, \quad (16)$$

where \tilde{E} is a sanitised version of E obtained by applying a light average-pool smoothing followed by threshold rescaling given by Eq. (17):

$$\tilde{E} = \left(\frac{\text{AvgPool}_3(E) - \tau}{1 - \tau} \right)_+, \quad (17)$$

with $\tau = 0.25$ and $(\cdot)_+ = \max(\cdot, 0)$ denotes rectification. The smoothing suppresses salt-and-pepper noise in the Sobel response, and the threshold τ discards weak gradients arising from background textures, retaining only strong, salient discontinuities as supervision targets. This term provides image-grounded boundary supervision that is independent of annotation quality, complementing $\mathcal{L}_{\text{gt-edge}}$ with a signal derived from raw image evidence.

Multi-scale aggregation and total objective All four terms are evaluated jointly across a set of spatial scales $\mathcal{S} = \{1.0, 0.5, 0.25\}$ with corresponding normalised weights $\omega = \{1.0, 0.25, 0.125\}$. At each scale $s \in \mathcal{S}$, the logit map z , the ground-truth mask y , and the edge prior E are bilinearly resampled to resolution $\lfloor sH \rfloor \times \lfloor sW \rfloor$. The scale-aggregated objective is defined in Eq. (18):

$$\mathcal{L}_{\text{ms}} = \frac{1}{\sum_s \omega_s} \sum_{s \in \mathcal{S}} \omega_s \left[\mathcal{L}_{\text{fs}}^{(s)} + \lambda_{\text{gt-edge}} \mathcal{L}_{\text{gt-edge}}^{(s)} + \lambda_{\text{ual}} \mathcal{L}_{\text{ual}}^{(s)} + \lambda_{\text{rgb}} \mathcal{L}_{\text{rgb}}^{(s)} \right] \quad (18)$$

where $\lambda_{\text{gt-edge}} = 0.01$, $\lambda_{\text{ual}} = 0.01$, and $\lambda_{\text{rgb}} = 0.005$ are fixed scalar coefficients. The coarser scales ($s \in \{0.5, 0.25\} \subset \mathcal{S}$) receive lower weights to ensure that the full-resolution supervision dominates, while still providing multi-scale gradient signal that stabilises training at early

diffusion timesteps. The final training objective is defined in Eq. (19):

$$\mathcal{L}_{\text{total}} = \mathcal{L}_{\text{ms}}, \quad (19)$$

which unifies region accuracy, boundary sharpness, uncertainty minimisation, and image-grounded contour alignment into a single, fully differentiable objective.

4. Experiments

4.1. Datasets

The method is evaluated on three widely used benchmarks for COD: CAMO [12], COD10K [5], and NC4K [15].

CAMO focuses on difficult real-world conditions. It features high visual ambiguity, with 82% depicting animals and 62% exhibiting extreme color similarity between target and background. Structural complexity is prevalent, as over 50% of images contain heavy background clutter or intricate boundaries. Also, 35% of images involve small objects (under 10% of the image area) and 29% present partial occlusions, adding further scale and visibility challenges.

COD10K is a large-scale benchmark featuring camouflaged animals across 78 categories in natural environments. Unlike earlier datasets, it exhibits minimal center bias with objects distributed more uniformly. It presents extreme scale variation, ranging from 0.01% to 80.74% of the image area, reflecting a realistic distribution. Global and local contrast levels indicate that COD10K presents higher visual difficulty compared to other benchmarks.

NC4K spans diverse scenarios, from naturally camouflaged animals to artificial objects. It presents high domain variability, featuring significant shifts in image quality, illumination, textures, and camouflage patterns. This, along with background clutter and scale diversity, frequently expose model weaknesses in boundary delineation and low-conspicuity detection. It serves as a rigorous benchmark for assessing robustness and cross-domain generalization.

4.2. Experimental setup

Following common practices, the training/validation subsets of CAMO and COD10K are merged, yielding 7,066 images in total. For in-distribution evaluation, the results are reported on the official test splits of the CAMO test set (250 images) and the COD10K test set (2,026 images) separately. To assess cross-dataset generalization, the model is evaluated on NC4K, which is not used for training. Model performance is assessed using four COD standard metrics: the Structure-measure (S_m), the weighted F-measure (F_β^w), the E-measure (E_m), and the Mean Absolute Error (MAE).

For training, each RGB image and its corresponding ground-truth mask are resized to 416×416 pixels. The training operates with 64 noise dimensions and 30 denoising steps at inference, predicting directly in x_0 space with

clipped denoising. Edge injection is configured with $\lambda_{inj} = 0.075$ and a Laplacian pre-filter, while the loss coefficients are set to $\lambda_{gt-edge} = 0.01$, $\lambda_{ual} = 0.01$, and $\lambda_{rgb} = 0.005$. The model is optimised with AdamW at a learning rate of 5×10^{-5} with cosine annealing over 150 epochs, using a batch size of 32 on two NVIDIA A100 GPUs of 24GB each.

4.3. Results and analysis

Results on CAMO Table 1 compares different edge extraction operators on CAMO. Canny, despite being the most sophisticated operator, ranks third behind Sobel and Laplacian of Gaussian (LoG). Sobel consistently outperforms all alternatives across every metric, with a 3% S_m gain and 0.009 MAE reduction over the weakest operator (Laplacian). This gap indicates that gradient smoothing before injection is the dominant factor, above operator complexity, which proves particularly effective under the complex structures present in CAMO.

Table 1. Ablation of edge prior extraction operators on CAMO dataset.

Edge method	$S_m \uparrow$	$E_m \uparrow$	$F_\beta^w \uparrow$	$MAE \downarrow$
Prewitt	0.8683	0.9314	0.8339	0.0448
Laplacian	0.8675	0.9267	0.8356	0.0483
Canny	0.8732	0.9335	0.8452	0.0439
LoG	0.8784	0.9410	0.8535	0.0416
Sobel	0.8971	0.9621	0.8740	0.0390

Table 2 ablates the proposed loss components on CAMO. Adding $\mathcal{L}_{gt-edge}$ alone to the multi-scale baseline temporarily drops performance, suggesting that boundary supervision without uncertainty regularisation introduces conflicting gradients under CAMO’s complex boundaries. \mathcal{L}_{ual} alone recovers this drop, and the combination of both restores and improves over the baseline. The full objective, incorporating \mathcal{L}_{rgb} as image-grounded boundary supervision, achieves the best results across all metrics, with a 2.4% S_m gain over the single-scale baseline, confirming that each component contributes to better optimising the model over the injected edge representations.

Table 2. Ablation of training losses under different combinations on CAMO dataset.

Loss	Components					Performance			
	\mathcal{L}_{fs}	MS	$\mathcal{L}_{gt-edge}$	\mathcal{L}_{ual}	\mathcal{L}_{rgb}	$S_m \uparrow$	$E_m \uparrow$	$F_\beta^w \uparrow$	$MAE \downarrow$
\mathcal{L}_{fs} (single-scale)	✓					0.8728	0.9325	0.8392	0.0450
\mathcal{L}_{fs} (multi-scale)	✓	✓				0.8732	0.9314	0.8443	0.0456
$\mathcal{L}_{fs} + \mathcal{L}_{gt-edge}$	✓	✓	✓			0.8650	0.9260	0.8321	0.0475
$\mathcal{L}_{fs} + \mathcal{L}_{ual}$	✓	✓		✓		0.8721	0.9317	0.8459	0.0450
$\mathcal{L}_{fs} + \mathcal{L}_{gt-edge} + \mathcal{L}_{ual}$	✓	✓	✓	✓		0.8783	0.9368	0.8517	0.0415
$\mathcal{L}_{fs} + \mathcal{L}_{gt-edge} + \mathcal{L}_{ual} + \mathcal{L}_{rgb}$	✓	✓	✓	✓	✓	0.8971	0.9621	0.8740	0.0390

Fig. 2 complements the quantitative results, illustrating how the proposed edge injection and boundary-supervised loss consistently produce sharper and more complete masks

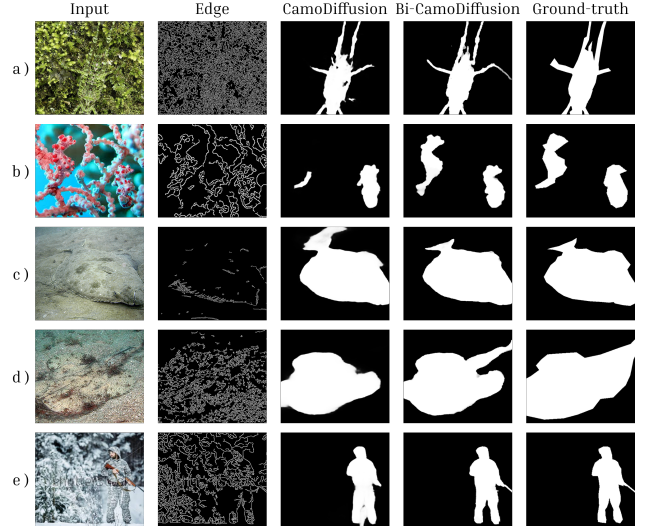


Figure 2. Qualitative comparison between our boundary-informed method and the baseline on the CAMO dataset.

compared to CamoDiffusion. The improvement is most evident in structurally challenging cases such as thin structures (a) and partially occluded objects (b), where the baseline either misses object parts or produces fragmented predictions, while our method recovers the full object extent more faithfully. Moreover, Table 3 shows that Bi-CamoDiffusion outperforms all compared methods on CAMO, confirming that the proposed edge injection and boundary-aware loss translate into consistent gains over the state-of-the-art (sota).

Table 3. Performance comparison of our approach with other methods from the state-of-the-art on CAMO dataset.

Method	$S_m \uparrow$	$E_m \uparrow$	$F_\beta^w \uparrow$	$MAE \downarrow$
EGNet [39]	0.7320	0.7996	0.6036	0.1095
PraNet [6]	0.7692	0.8245	0.6625	0.0942
F ³ Net [31]	0.7113	0.7407	0.5636	0.1087
MINet [19]	0.7480	0.7911	0.6370	0.0903
SINet [5]	0.7454	0.8035	0.6443	0.0915
C ² F-Net [28]	0.7961	0.8537	0.7187	0.0799
PFNet [18]	0.7823	0.8410	0.6952	0.0849
MGL [37]	0.7755	0.8160	0.6728	0.0884
UGTR [34]	0.7839	0.8215	0.6836	0.0863
SINet-v2 [7]	0.8201	0.8817	0.7426	0.0705
BASNet [22]	0.7943	0.8511	0.7174	0.0786
OCENet [14]	0.8019	0.8518	0.7234	0.0804
BGNet [29]	0.8116	0.8698	0.7485	0.0734
ZoomNet [20]	0.8197	0.8770	0.7522	0.0659
CamoDiffusion [2]	0.8659	0.9238	0.8263	0.0480
FSEL [30]	0.8850	0.9420	0.8500	0.0400
Bi-CamoDiffusion	0.8971	0.9621	0.8740	0.0390

Results on COD10K Table 4 reports the edge operators ablation on COD10K. Sobel again leads across all metrics, and the trend observed on CAMO is largely consistent here. Notably, the performance spread across operators is narrower than on CAMO, with a 1.7% S_m gap between So-

bel and the weakest operator, suggesting that on COD10K’s highly variable object scales the choice of edge operator has less impact than in CAMO’s structurally complex scenes.

Table 4. Ablation of edge prior extraction operators on COD10K dataset.

Edge method	$S_m \uparrow$	$E_m \uparrow$	$F_\beta^w \uparrow$	$MAE \downarrow$
Prewitt	0.8647	0.9280	0.7848	0.0231
Laplacian	0.8720	0.9303	0.7967	0.0230
Canny	0.8693	0.9373	0.8103	0.0228
LoG	0.8781	0.9338	0.8053	0.0230
Sobel	0.8813	0.9491	0.8343	0.0200

Table 5 reports the loss ablation on COD10K. The pattern mirrors CAMO in that $\mathcal{L}_{gt-edge}$ alone temporarily hurts performance. A notable finding is that on COD10K, where objects span extreme scale variation, \mathcal{L}_{ual} proves particularly impactful, recovering and surpassing the baseline even without $\mathcal{L}_{gt-edge}$, suggesting that uncertainty regularisation is especially beneficial when the model must handle highly variable object sizes. The full objective again achieves the best results across all metrics, with \mathcal{L}_{rgb} providing the final gain that consolidates all boundary supervision signals.

Table 5. Ablation of training losses under different combinations on COD10K dataset.

Loss	Components				Performance				
	\mathcal{L}_{fs}	MS	$\mathcal{L}_{gt-edge}$	\mathcal{L}_{ual}	\mathcal{L}_{rgb}	$S_m \uparrow$	$E_m \uparrow$	$F_\beta^w \uparrow$	$MAE \downarrow$
\mathcal{L}_{fs} (single-scale)	✓					0.8715	0.9307	0.7918	0.0219
\mathcal{L}_{fs} (multi-scale)	✓					0.8715	0.9332	0.7918	0.0218
$\mathcal{L}_{fs} + \mathcal{L}_{gt-edge}$	✓	✓				0.8686	0.9260	0.8004	0.0224
$\mathcal{L}_{fs} + \mathcal{L}_{ual}$	✓	✓		✓		0.8745	0.9314	0.8102	0.0210
$\mathcal{L}_{fs} + \mathcal{L}_{gt-edge} + \mathcal{L}_{ual}$	✓	✓	✓	✓		0.8734	0.9367	0.8240	0.0209
$\mathcal{L}_{fs} + \mathcal{L}_{gt-edge} + \mathcal{L}_{ual} + \mathcal{L}_{rgb}$	✓	✓	✓	✓	✓	0.8813	0.9491	0.8343	0.0200

Likewise, Fig. 3 shows qualitative results on COD10K, where the proposed method more accurately delineates fragmented structures (c) and objects with complex, multi-pronged boundaries (b, d), while CamoDiffusion struggles to recover the full structural detail. Similarly, Table 6 confirms that Bi-CamoDiffusion leads across all metrics on COD10K, achieving notable gains over ZoomNet, BGNet and CamoDiffusion in S_m , E_m and F_β^w . FSEL, despite ranking second and outperforming all other competing methods, does not reach the levels achieved by Bi-CamoDiffusion, with S_m and E_m below 0.88 and 0.93 respectively, reflecting weaker structural understanding and contour alignment on this benchmark.

Results on NC4K Table 7 compares edge extraction operators on NC4K. Sobel maintains its lead across all metrics, with a 2% S_m gain over Prewitt and the lowest MAE overall, showing that Sobel-extracted edge priors provide the most effective boundary cues for our model to generalise to unseen domains. Despite a competitive MAE, Canny edges

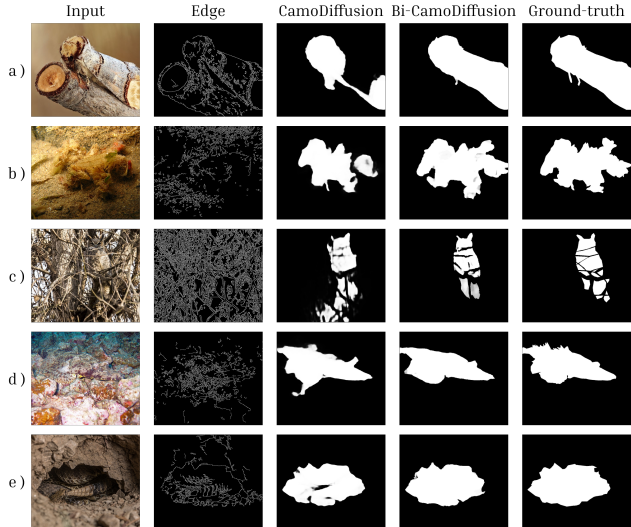


Figure 3. Qualitative comparison between our boundary-informed method and the baseline on the COD10K dataset.

Table 6. Performance comparison of our approach with other methods from the state-of-the-art on COD10K dataset.

Method	$S_m \uparrow$	$E_m \uparrow$	$F_\beta^w \uparrow$	$MAE \downarrow$
EGNet [39]	0.7365	0.8097	0.5174	0.0607
PraNet [6]	0.7894	0.8606	0.6294	0.0451
F ³ Net [31]	0.7386	0.7951	0.5438	0.0513
MINet [19]	0.7697	0.8320	0.6085	0.0417
SINet [5]	0.7794	0.8642	0.6310	0.0426
C ² F-Net [28]	0.8130	0.8902	0.6862	0.0360
PFNet [18]	0.7998	0.8772	0.6599	0.0396
MGL [37]	0.8139	0.8513	0.6657	0.0353
UGTR [34]	0.8171	0.8519	0.6656	0.0356
SINet-v2 [7]	0.8151	0.8870	0.6796	0.0368
BASNet [22]	0.8176	0.8905	0.6990	0.0342
OCENet [14]	0.8272	0.8935	0.7071	0.0327
BGNet [29]	0.8307	0.9007	0.7219	0.0326
ZoomNet [20]	0.8384	0.8876	0.7288	0.0289
CamoDiffusion [2]	0.8599	0.9274	0.7732	0.0245
FSEL [30]	0.8730	0.9280	0.8000	0.0210
Bi-CamoDiffusion	0.8813	0.9491	0.8343	0.0200

yield the weakest F_β^w , suggesting that they are less informative for detection under NC4K’s high variability.

Table 7. Ablation of edge prior extraction operators on NC4K dataset.

Edge method	$S_m \uparrow$	$E_m \uparrow$	$F_\beta^w \uparrow$	$MAE \downarrow$
Prewitt	0.8842	0.9337	0.8246	0.0321
Laplacian	0.8910	0.9173	0.8102	0.0314
Canny	0.8975	0.9256	0.8001	0.0310
LoG	0.9001	0.9307	0.8234	0.0345
Sobel	0.9043	0.9532	0.8517	0.0209

Also, Table 8 shows the loss ablation on NC4K. The full objective is the only configuration to surpass 0.90 S_m and 0.95 in E_m , indicating that the complete loss enables the model to capture the structural composition of camou-

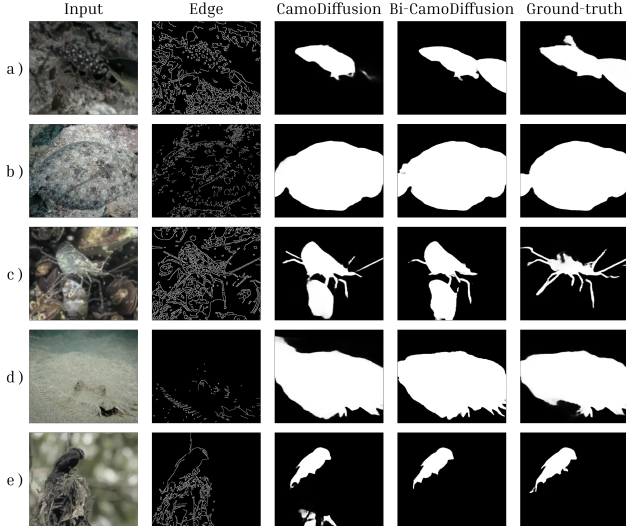


Figure 4. Qualitative comparison between our boundary-informed method and the baseline on the NC4K dataset.

flaged objects more accurately, which no partial combination achieves in this unseen domain. The remaining metrics also improve progressively, confirming that the boundary supervision introduced by each term transfers beyond the training distribution.

Table 8. Ablation of training losses under different combinations on NC4K dataset.

Loss	Components					Performance			
	\mathcal{L}_{fs}	MS	$\mathcal{L}_{gt-edge}$	\mathcal{L}_{ual}	\mathcal{L}_{rgb}	$S_m \uparrow$	$E_m \uparrow$	$F_{\beta}^w \uparrow$	MAE \downarrow
\mathcal{L}_{fs} (single-scale)	✓					0.8874	0.9365	0.8225	0.0319
\mathcal{L}_{fs} (multi-scale)	✓	✓				0.8880	0.9389	0.8250	0.0302
$\mathcal{L}_{fs} + \mathcal{L}_{gt-edge}$	✓	✓	✓			0.8890	0.9377	0.8129	0.0300
$\mathcal{L}_{fs} + \mathcal{L}_{ual}$	✓	✓		✓		0.8889	0.9282	0.8269	0.0263
$\mathcal{L}_{fs} + \mathcal{L}_{gt-edge} + \mathcal{L}_{ual}$	✓	✓	✓	✓		0.8899	0.9383	0.8358	0.0297
$\mathcal{L}_{fs} + \mathcal{L}_{gt-edge} + \mathcal{L}_{ual} + \mathcal{L}_{rgb}$	✓	✓	✓	✓	✓	0.9043	0.9532	0.8517	0.0209

Fig. 4 shows qualitative results on NC4K. More difficulty is observed in generating accurate masks in this unseen domain, yet the proposed method consistently produces fewer false positive regions (b, d and e), with notably better delineation of small and elongated details, as evident in (e). Finally, Table 9 confirms this against the sota, with Bi-CamoDiffusion being the only method to surpass 0.90 in S_m , 0.95 in E_m , and achieve a MAE below 0.03, demonstrating superior structural understanding and contour precision even under the domain shift conditions of NC4K.

5. Limitations and future work

Despite evaluating Bi-CamoDiffusion on multiple datasets and against different competing methods, some limitations of this study must be acknowledged. First, our evaluation follows the official splits provided by each benchmark. While this ensures comparability with prior work, it does

Table 9. Performance comparison of our approach with other methods from the state-of-the-art on NC4K dataset.

Method	$S_m \uparrow$	$E_m \uparrow$	$F_{\beta}^w \uparrow$	MAE \downarrow
EGNet [39]	0.7771	0.8408	0.6386	0.0751
PraNet [6]	0.8222	0.8761	0.7245	0.0588
F ³ Net [31]	0.7800	0.8244	0.6556	0.0695
MINet [19]	0.8122	0.8618	0.7195	0.0555
SINet [5]	0.8080	0.8173	0.7227	0.0576
C ² F-Net [28]	0.8383	0.8974	0.7624	0.0490
PFNet [18]	0.8290	0.8874	0.7453	0.0527
MGL [37]	0.8326	0.8666	0.7392	0.0526
UGTR [34]	0.8394	0.8744	0.7463	0.0519
SINet-v2 [7]	0.8472	0.9027	0.7698	0.0476
BASNet [22]	0.8414	0.8968	0.7708	0.0479
OCENet [14]	0.8533	0.9025	0.7846	0.0450
BGNet [29]	0.8510	0.9067	0.7884	0.0444
ZoomNet [20]	0.8528	0.8957	0.7844	0.0434
CamoDiffusion [2]	0.8833	0.9343	0.8372	0.0325
FSEL [30]	0.8920	0.9410	0.8530	0.0300
Bi-CamoDiffusion	0.9043	0.9532	0.8517	0.0209

not include targeted analyses of specific COD conditions, such as naturally and artificially camouflaged cases separately. Future work could expand the evaluation to specific scenarios of interest. Likewise, a natural direction for future work is to test alternative methods for extracting the edge prior. This study primarily relied on classical image-processing operators; therefore, more advanced alternatives can be explored, including deep learning-based edge or contour detectors that may provide stronger and more semantically consistent boundary cues. Another promising direction is to extend the model design beyond a fixed, parameter-free prior injection by incorporating priors through lightweight, learnable integration modules and analyzing the impact of such an approach.

6. Conclusions

This work introduces Bi-CamoDiffusion, a boundary-informed diffusion model for Camouflaged Object Detection. The original CamoDiffusion is extended by incorporating a parameter-free prior injection process that modulates early-stage embeddings with edge-aware information. Furthermore, a loss function is proposed that combines spatial precision, structural edge constraints, and uncertainty-aware supervision into a unified objective to ensure the model captures both global semantics and local boundary details. Experiments on CAMO, COD10K, and NC4K datasets demonstrate that Bi-CamoDiffusion achieves a significant improvement in object delineation, producing finer detections and a notable reduction in false positives. Also, our model consistently outperforms existing state-of-the-art methods, demonstrating superior boundary precision and a deeper structural understanding.

References

- [1] Geng Chen, Si-Jie Liu, Yu-Jia Sun, Ge-Peng Ji, Ya-Feng Wu, and Tao Zhou. Camouflaged object detection via context-aware cross-level fusion. *IEEE TCSVT*, 32(10):6981–6993, 2022. 1
- [2] Zhongxi Chen, Ke Sun, and Xianming Lin. Camodiffusion: Camouflaged object detection via conditional diffusion models. In *AAAI*, 2024. 1, 2, 6, 7, 8
- [3] Runmin Cong, Mengyao Sun, Sanyi Zhang, Xiaofei Zhou, Wei Zhang, and Yao Zhao. Frequency perception network for camouflaged object detection. In *ACMMM*, 2023. 2
- [4] Ji Du, Xin Wang, Fangwei Hao, Mingyang Yu, Chunyuan Chen, Jiesheng Wu, Bin Wang, Jing Xu, and Ping Li. Beyond single images: Retrieval self-augmented unsupervised camouflaged object detection. In *ICCV*, 2025. 2
- [5] Deng-Ping Fan, Ge-Peng Ji, Guolei Sun, Ming-Ming Cheng, Jianbing Shen, and Ling Shao. Camouflaged object detection. In *CVPR*, 2020. 5, 6, 7, 8
- [6] Deng-Ping Fan, Ge-Peng Ji, Tao Zhou, Geng Chen, Huazhu Fu, Jianbing Shen, and Ling Shao. Pranet: Parallel reverse attention network for polyp segmentation. In *MICCAI*, 2020. 6, 7, 8
- [7] Deng-Ping Fan, Ge-Peng Ji, Ming-Ming Cheng, and Ling Shao. Concealed object detection. *IEEE TPAMI*, 44(10):6024–6042, 2022. 1, 6, 7, 8
- [8] Chunming He, Kai Li, Yachao Zhang, Longxiang Tang, Yulun Zhang, Zhenhua Guo, and Xiu Li. Camouflaged object detection with feature decomposition and edge reconstruction. In *CVPR*, 2023. 1, 2
- [9] Chunming He et al. Strategic preys make acute predators: Enhancing camouflaged object detectors by generating camouflaged objects. In *ICLR*, 2024. 2
- [10] Jonathan Ho, Ajay Jain, and Pieter Abbeel. Denoising diffusion probabilistic models. In *NeurIPS*, 2020. 1
- [11] Ge-Peng Ji, Deng-Ping Fan, Yu-Cheng Chou, Dengxin Dai, Alexander Liniger, and Luc Van Gool. Deep gradient learning for efficient camouflaged object detection. *Mach. Intell. Res.*, 20(1):92–108, 2023. 1
- [12] Trung-Nghia Le, Tam V. Nguyen, Zhongliang Nie, Minh-Triet Tran, and Akihiro Sugimoto. Anabran network for camouflaged object segmentation. *Computer Vision and Image Understanding*, 184:45–56, 2019. 5
- [13] Yanhua Liang, Guihe Qin, Minghui Sun, Xinchao Wang, Jie Yan, and Zhonghan Zhang. A systematic review of image-level camouflaged object detection with deep learning. *Neurocomputing*, 566:127050, 2024. 1
- [14] Jiawei Liu, Jing Zhang, and Nick Barnes. Modeling aleatoric uncertainty for camouflaged object detection. In *WACV*, 2022. 6, 7, 8
- [15] Yunqiu Lv, Jing Zhang, Yuchao Dai, Aixuan Li, Bowen Liu, Nick Barnes, and Deng-Ping Fan. Simultaneously localize, segment and rank the camouflaged objects. In *CVPR*, 2021. 2, 5
- [16] Yunqiu Lv et al. Segment, magnify and reiterate: Detecting camouflaged objects the hard way. In *CVPR*, 2022. 2
- [17] Manuel Madeira, Clément Vignac, Dorina Thanou, and Pascal Frossard. Generative modelling of structurally constrained graphs. In *NeurIPS*, 2024. 1
- [18] Haiyang Mei, Ge-Peng Ji, Ziqi Wei, Xin Yang, Xiaopeng Wei, and Deng-Ping Fan. Camouflaged object segmentation with distraction mining. In *CVPR*, 2021. 6, 7, 8
- [19] Youwei Pang, Xiaoqi Zhao, Lihe Zhang, and Huchuan Lu. Multi-scale interactive network for salient object detection. In *CVPR*, 2020. 6, 7, 8
- [20] Youwei Pang, Xiaoqi Zhao, Tian-Zhu Xiang, Lihe Zhang, and Huchuan Lu. Zoom in and out: A mixed-scale triplet network for camouflaged object detection. In *CVPR*, 2022. 6, 7, 8
- [21] Youwei Pang, Xiaoqi Zhao, Tian-Zhu Xiang, Lihe Zhang, and Huchuan Lu. Zoomnext: A unified collaborative pyramid network for camouflaged object detection. *IEEE TPAMI*, 46(12):9205–9220, 2024. 2
- [22] Xuebin Qin, Zichen Zhang, Chenyang Huang, Chao Gao, Masood Dehghan, and Martin Jagersand. Basnet: Boundary-aware salient object detection. In *CVPR*, 2019. 6, 7, 8
- [23] Leo Thomas Ramos and Angel D. Sappa. Multispectral semantic segmentation for land cover classification: An overview. *IEEE JSTARS*, 17:14295–14336, 2024. 1
- [24] Leo Thomas Ramos and Angel D. Sappa. Exploring diffusion-generated guidance for thermal image super-resolution. In *WACVW*, 2026. 1
- [25] Jingjing Ren, Xiaowei Hu, Lei Zhu, Xuemiao Xu, Yangyang Xu, Weiming Wang, Zijun Deng, and Pheng-Ann Heng. Deep texture-aware features for camouflaged object detection. *IEEE TCSVT*, 33(3):1157–1167, 2023. 1
- [26] Jiaming Song, Chenlin Meng, and Stefano Ermon. Denoising diffusion implicit models. In *ICLR*, 2021. 1
- [27] Patricia L. Suárez and Angel D. Sappa. Edge-aware camouflaged object detection. In *CAIP*, 2026. 1
- [28] Yujia Sun, Geng Chen, Tao Zhou, Yi Zhang, and Nian Liu. Context-aware cross-level fusion network for camouflaged object detection. In *IJCAI*, 2021. 2, 6, 7, 8
- [29] Yujia Sun, Shuo Wang, Chenglizhao Chen, and Tian-Zhu Xiang. Boundary-guided camouflaged object detection. In *IJCAI*, 2022. 6, 7, 8
- [30] Yanguang Sun, Chunyan Xu, Jian Yang, Hanyu Xuan, and Lei Luo. Frequency-spatial entanglement learning for camouflaged object detection. In *ECCV*, 2024. 2, 6, 7, 8
- [31] Jun Wei, Shuhui Wang, and Qingming Huang. F³net: Fusion, feedback and focus for salient object detection. In *AAAI*, 2020. 6, 7, 8
- [32] Haoyu Wu, Diankun Wu, Tianyu He, Junliang Guo, Yang Ye, Yueqi Duan, and Jiang Bian. Geometry forcing: Marrying video diffusion and 3d representation for consistent world modeling. *arXiv preprint arXiv:2507.07982*, 2025. 1
- [33] Weiqi Yan, Lvhai Chen, Shengchuan Zhang, Yan Zhang, and Liujuan Cao. Scout: Semi-supervised camouflaged object detection by utilizing text and adaptive data selection. In *IJCAI*, 2025. 2
- [34] Fan Yang, Qiang Zhai, Xin Li, Rui Huang, Ao Luo, Hong Cheng, and Deng-Ping Fan. Uncertainty-guided transformer reasoning for camouflaged object detection. In *ICCV*, 2021. 2, 6, 7, 8

- [35] Yang Yang and Qiang Zhang. Finding camouflaged objects along the camouflage mechanisms. *IEEE TCSVT*, 34(4): 2346–2360, 2024. [1](#)
- [36] Bowen Yin, Xuying Zhang, Deng-Ping Fan, Shaohui Jiao, Ming-Ming Cheng, Luc Van Gool, and Qibin Hou. Camoformer: Masked separable attention for camouflaged object detection. *IEEE TPAMI*, 46(12):10362–10374, 2024. [2](#)
- [37] Qiang Zhai, Xin Li, Fan Yang, Chenglizhao Chen, Hong Cheng, and Deng-Ping Fan. Mutual graph learning for camouflaged object detection. In *CVPR*, 2021. [1](#), [2](#), [6](#), [7](#), [8](#)
- [38] Jin Zhang, Ruiheng Zhang, Yanjiao Shi, Zhe Cao, Nian Liu, and Fahad Shahbaz Khan. Learning camouflaged object detection from noisy pseudo label. In *ECCV*, 2024. [2](#)
- [39] Jiaxing Zhao, Jiang-Jiang Liu, Deng-Ping Fan, Yang Cao, Jufeng Yang, and Ming-Ming Cheng. Egnnet: Edge guidance network for salient object detection. In *ICCV*, 2019. [6](#), [7](#), [8](#)
- [40] Junmin Zhong, Anzhi Wang, Chunhong Ren, and Jintao Wu. A survey on deep learning-based camouflaged object detection. *Multimed. Syst.*, 30(5), 2024. [1](#)